Supplementary Information (SI)

Beyond the Surface: Inferring Internal Battery Pressure and Temperature Using Optical Fibre Sensing and Machine Learning

Lucca Matuck[1], João P. Pires[1], José F. F. Mendes[1], Marta S. Ferreira[1], Micael Nascimento[1]*

[1]i3N and Department of Physics, University of Aveiro, Campus de Santiago, 3810-193 Aveiro, Portugal

*Corresponding author: micaelnascimento@ua.pt

Supplementary Tables

Table S1 Optimised hyperparameters of the temporal models. Summary of the Temporal Convolutional Network (TCN) configurations obtained via Bayesian optimisation for each chemistry, where a single model jointly predicts internal temperature (T_{in}) and internal pressure variation (ΔP_{in}). The table reports the input window length, number of convolutional filters, kernel size, dense-layer units, dropout rate, batch size, and learning rate used throughout the main text. Each optimisation comprised 500 trials per chemistry (seed = 42).

Chemistry	Window length	TCN filters	Dense units	Kernel size	Dropout	Batch size	Learning Rate
Li-ion	20	128	32	9	0.100	64	0.0014
Na-ion	30	64	48	3	0.285	16	0.0023

Table S2 Global performance metrics for all models. Comprehensive error statistics for the LIB and SIB virtual-sensing models. For each chemistry and target variable, the table reports mean absolute error (MAE), root mean squared error (RMSE), median absolute error (MedAE), mean/standardised normalised RMSE (including $NRMSE_{std}$ and $NRMSE_{range}$) and coefficient of determination (R^2) computed on the held-out test cycles. These values underpin the parity plots in Fig. 3.

Chemistry	Target	MAE (°C / bar)	RMSE (°C / bar)	MedAE (°C / bar)	$NRMSE_{std}$	$NRMSEr_{ange}$ (%)	R^2
Li-ion	T_{in}	0.058	0.075	0.047	0.059	1.17	0.996
Li-ion	ΔP_{in}	0.028	0.048	0.012	0.170	4.25	0.971
Na-ion	T_{in}	0.202	0.288	0.143	0.102	1.87	0.990
Na-ion	ΔP_{in}	0.011	0.013	0.009	0.299	5.34	0.911

Supplementary Figures

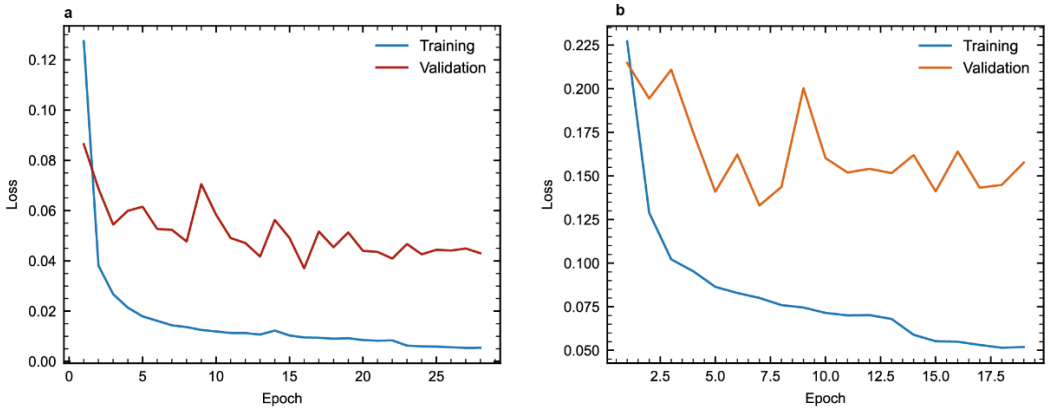

Fig. S1 Training and validation loss curves for LIB and SIB models. **a.** Evolution of training and validation losses for the LIB models predicting internal temperature and pressure over the training epochs. **b.** Corresponding loss curves for the SIB models. In both chemistries, training loss decreases steadily, whereas validation loss improves primarily during the early epochs and then fluctuates around a plateau, revealing a train–validation gap but no late-epoch instability.

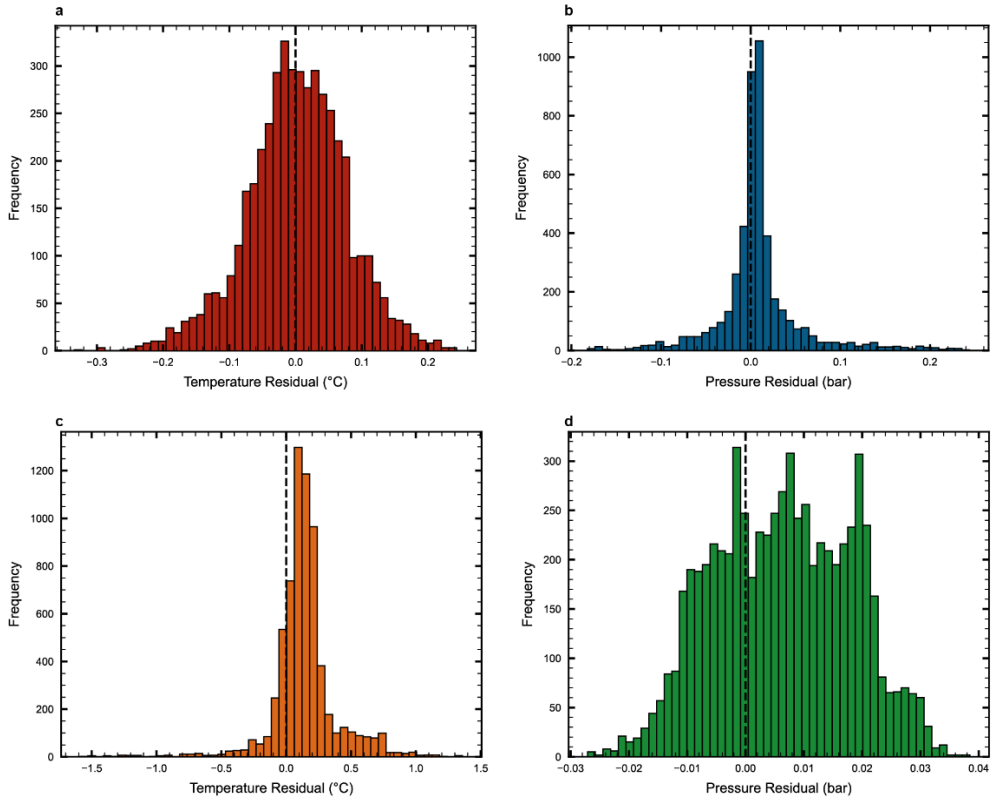

Fig. S2 Histograms of residuals for internal temperature and pressure. **a.** Distribution of residuals (prediction minus ground truth) for LIB internal temperature on the test set. **b.** Residual distribution for LIB internal pressure. **c.** and **d.** Corresponding histograms for SIB internal temperature and pressure, respectively. Histograms are centred approximately around zero for all tasks, with narrower spreads for temperature than

for pressure, and slightly heavier tails for pressure residuals. These distributions complement the parity plots in Fig. 3 and the residual maps in Fig. 4, illustrating the overall symmetry and magnitude of the errors.

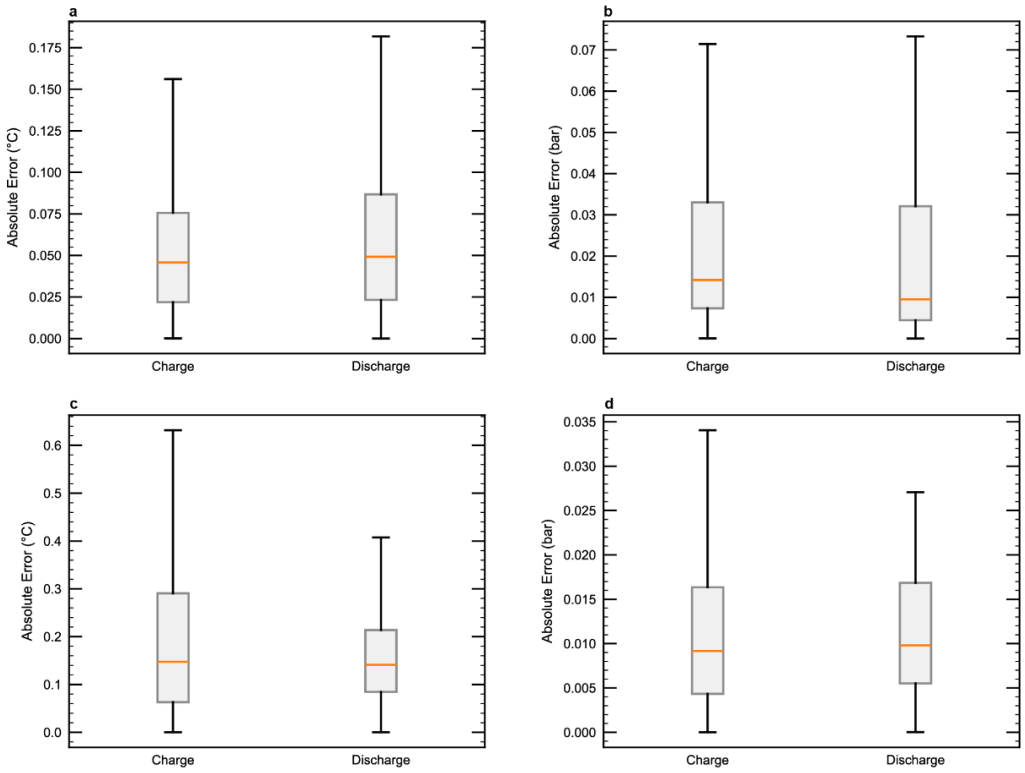

Fig. S3 Charge/discharge-resolved absolute errors. **a.** Boxplots of the absolute error in LIB internal temperature, separated into charge and discharge segments for the test cycles. **b.** Equivalent boxplots for LIB internal pressure. **c.** and **d.** Corresponding charge/discharge-resolved boxplots for SIB internal temperature and pressure. The distributions show comparable median errors and variability between charge and discharge, indicating that model performance is robust across operating directions and is not dominated by a specific regime. These results support the discussion of regime-independent accuracy in Section 2.4.

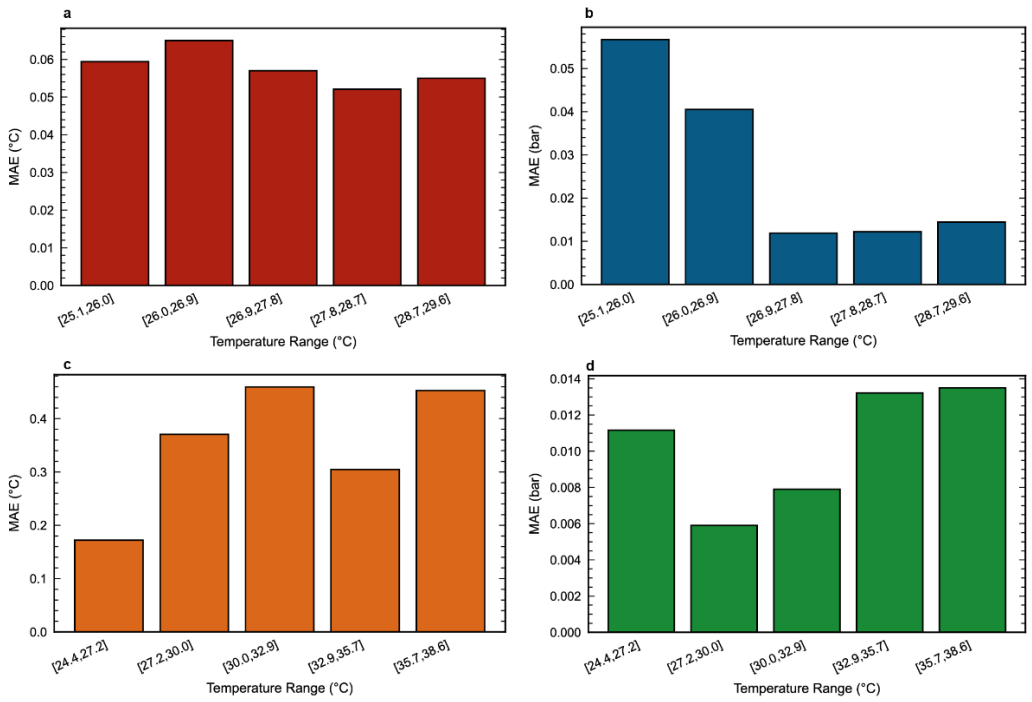

Fig. S4 Range-wise error as a function of internal temperature. **a.** MAE of LIB internal temperature predictions as a function of true internal-temperature range. **b.** Range-wise error profiles for LIB internal pressure. **c.** and **d.** Analogous temperature-binned error profiles for SIB internal temperature and pressure. The curves reveal how prediction errors evolve across the explored temperature range, showing that LIB errors remain nearly uniform, whereas SIB temperature errors exhibit a moderate increase at higher temperatures. These observations are referenced in Section 2.4 when analysing error dependence on thermal conditions.

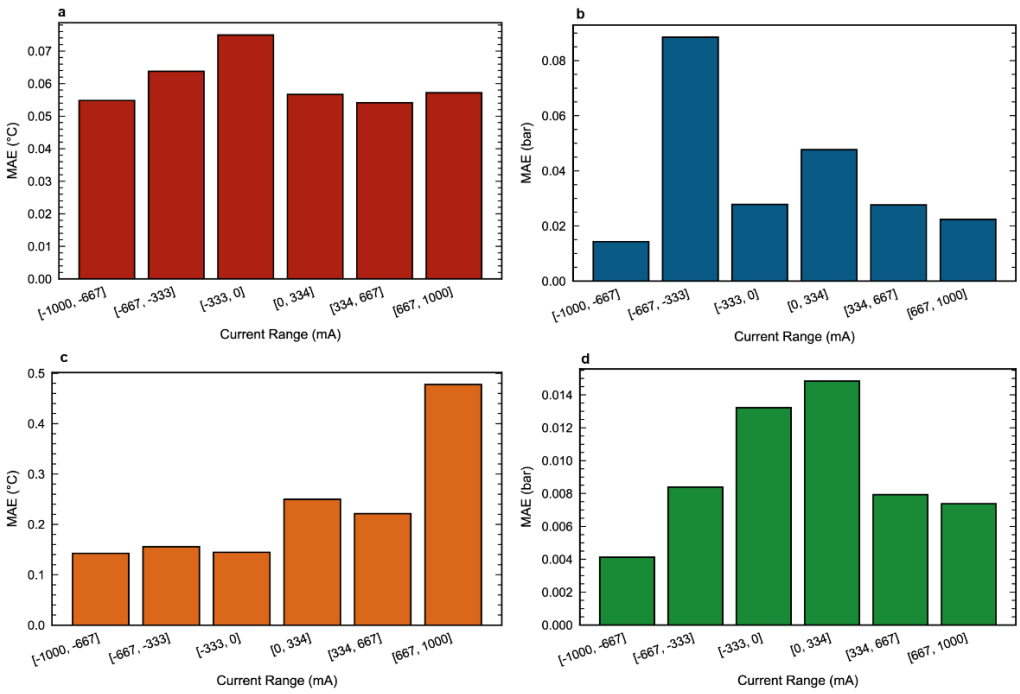

Fig. S5 Range-wise error as a function of current. **a.** MAE of LIB internal temperature as a function of current range, computed over test-set segments grouped by applied current. **b.** Corresponding current-binned errors for LIB internal pressure. **c.** and **d.** Analogous current-range error profiles for SIB internal temperature and pressure. The plots demonstrate that temperature errors tend to increase at higher currents, reflecting stronger dynamical excitation, while pressure errors show limited dependence on current across the investigated ranges. These trends complement the temperature-binned analysis in Supplementary Fig. S4 and support the statements in Section 2.4 regarding the operating-condition dependence of the residuals.

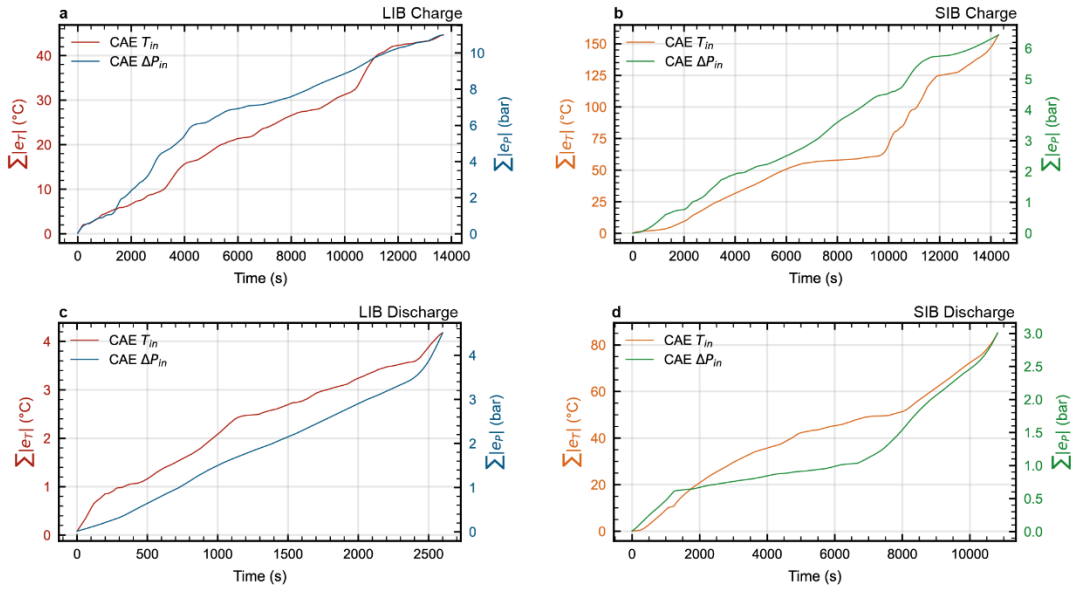

Fig. S6 a. Cycle-resolved cumulative absolute error (CAE) for internal temperature and pressure. CAE over time for T_{in} and ΔP_{in} during the same representative charge and discharge test cycles shown in Fig. 5. Panels show charge (a,b) and discharge (c,d) cycles for LIB (a,c) and SIB (b,d) cells. For each target, the CAE is computed as the running sum of |e(t)| along the cycle. The approximately linear growth and absence of abrupt jumps indicate that errors remain bounded and do not accumulate catastrophically over time, supporting temporal stability over unseen test cycles.